

THE ULTRA-LONG GRB 111209A. II. PROMPT TO AFTERGLOW AND AFTERGLOW PROPERTIES

G. STRATTA¹, B. GENDRE², J. L. ATTEIA^{3,4}, M. BOËR², D. M. COWARD⁵, M. DE PASQUALE⁶,
 E. HOWELL⁵, A. KLOTZ⁷, S. OATES⁶, AND L. PIRO⁸

¹ Osservatorio Astronomico di Roma (OAR/INAF), via Frascati 33, I-00040 Monte Porzio Catone, Italy

² ARTEMIS, UMR 7250 (CNRS/OCA/UNS), boulevard de l’Observatoire, BP 4229, F-06304 Nice Cedex, France

³ Université de Toulouse, UPS-OMP, IRAP, F-31400 Toulouse, France

⁴ CNRS, IRAP, 14, avenue Edouard Belin, F-31400 Toulouse, France

⁵ School of Physics, University of Western Australia (UWA), Crawley, WA 6009, Australia

⁶ Mullard Space Science Laboratory (MSSL), University College London, Holmbury St. Mary, Dorking, Surrey RH5 6NT, UK

⁷ IRAP, 14, avenue Edouard Belin, F-31400 Toulouse, France

⁸ Istituto di Astrofisica e Planetologia Spaziali di Roma (IAPS/INAF), via fosso del cavaliere 100, I-00133 Roma, Italy

Received 2013 June 6; accepted 2013 September 26; published 2013 November 26

ABSTRACT

The “ultra-long” gamma-ray burst GRB 111209A at redshift $z = 0.677$ is the longest GRB ever observed thus far, with a rest frame prompt emission duration of ~ 4 hr. In order to explain the burst exceptional longevity, a low-metallicity blue supergiant progenitor was invoked. In this article we further constrain the phenomenology and progenitor properties of this peculiar GRB by performing a multiband temporal and spectral analysis of both the prompt and the afterglow emission. We use proprietary and publicly available data from *Swift*, *Konus WIND*, *XMM-Newton*, and TAROT, as well as from other ground-based optical and radio telescopes. We find some peculiar properties that are possibly connected to the exceptional nature of this burst, namely: (1) an unprecedented large optical delay of 410 ± 50 s between the peak time in gamma-rays and the peak time in the optical of a marked multiwavelength flare; (2) multiwavelength prompt emission spectral modeling requires a certain amount of dust in the circumburst environment. The dust produces a rest frame visual extinction of $A_V = 0.3\text{--}1.5$ mag, and may undergo destruction at late times; and (3) we detect the presence of a hard spectral extra power-law component at the end of the X-ray steep decay phase and before the start of the X-ray afterglow, which has never been revealed thus far in past GRBs. The optical afterglow shows more usual properties; it has a flux power-law decay with an index of 1.6 ± 0.1 and a late rebrightening feature observed at ~ 1.1 the day after the first Burst Alert Telescope trigger. We discuss our findings in the context of several possible interpretations that have been given thus far of the complex multiband GRB phenomenology and propose a binary channel formation for the blue supergiant progenitor.

Key words: gamma-ray burst: general – gamma-ray burst: individual (GRB 111209A)

Online-only material: color figures

1. INTRODUCTION

Long gamma-ray bursts (LGRBs) are commonly interpreted in the context of the collapsar model (Woosley 1993; Paczynski 1998; MacFadyen & Woosley 1999; Woosley & Bloom 2006), where a massive, highly rotating star collapses into a black hole or a neutron star (NS) and forms a temporary torus of matter around the central object. In this scenario, the accretion onto the central object is the engine that produces a burst of radiation expected to last from a few seconds to a few tens of seconds. The typical durations of GRB prompt emission at high energy have a distribution that peaks at 20–30 s, with a range that goes from a few seconds up to hundreds of seconds (Kouveliotou et al. 1993). This is consistent with the expected time scale of a gravitational collapse of the core of a massive star such as the Carbon–Oxygen Wolf–Rayet (WR) star.

GRB 111209A was an exceptional “ultra-long” GRB at redshift $z = 0.677$ (Vreeswijk et al. 2011), with an unprecedented burst duration of a few hours (Hoversten et al. 2011a). The existence of ultra-long bursts such as GRB 111209A, together with other very long GRBs, for example, GRB 101225 and GRB 121027A (e.g., Levan et al. 2013), has imposed some modifications to the standard collapsar model mentioned above. Among the scenarios proposed to explain these events are a more massive and extended progenitor star (e.g., Gendre et al. 2013; Nakauchi et al. 2013) or fall-back accretion of a partly

survived progenitor envelope (e.g., Wu et al. 2013; Quataert & Kasen 2012).

Motivated by the unique properties of the prompt emission of GRB 111209A, we proposed (Gendre et al. 2013, hereafter Paper I) that this burst could originate from a blue supergiant, a hypothesis that has been further investigated by Nakauchi et al. (2013). Indeed, following Woosley & Heger (2012), we found in Paper I that the long duration and high luminosity of GRB 111209A in gamma rays and the lack of evidence of a bright supernova (SN) during the successful follow-up campaign up to dozens of days after the trigger (despite the rather low redshift of this burst; see Levan et al. 2013) favor a rare type of low-metallicity collapsing blue supergiant as progenitor. If true, bursts like GRB 111209A would be a better prototype of the expected Pop III stars than normal LGRBs (e.g., Kashiyama et al. 2013). GRB 111209A cannot be considered an extreme representative of the LGRB class, and we showed evidence in Paper I for which we had to invoke a different progenitor. This is also the conclusion reached later by Levan et al. (2013).

In this article we investigate the global properties of GRB 111209A, taking advantage of the extended data set that we were able to acquire both during the prompt phase and the afterglow. We show that while there are some similarities of the multiwavelength afterglow emission with “normally” LGRBs, the prompt emission and the prompt-to-afterglow transition present

peculiar properties. The overall picture emerging from our analysis supports the evidence of a non-negligible metallicity in the host galaxy (Levan et al. 2013). We tentatively suggest a binary system progenitor for GRB 111209A to address the metal-enriched environment.

In the following sections we present the data set we used in our analysis (Section 2) and the temporal and spectral properties of the prompt emission (Section 3) and of the early and late afterglow (Section 4). We then discuss our findings (Section 5) and present our conclusions (Section 6).

Throughout the article, we describe the temporal and spectral power-law indices according to the notation $F(\nu, t) \propto \nu^{-\beta} t^{-\alpha}$, unless otherwise specified.

2. THE DATA

The Burst Alert Telescope (BAT) coded mask telescope on board *Swift* was triggered twice by GRB 111209A on 2011 December 9 at $T_0 = 07:12:08$ UT and on $T_0 + 424$ s (trigger numbers 509336 and 509337). The *Swift* X-Ray Telescope (XRT) monitoring started at $T_0 + 419$ s, and the UV-optical telescope (UVOT) began settled observations at 427 s post trigger (Hoversten et al. 2011b). Simultaneous *R*-band observations were performed with the TAROT ESO (Chile) robotic telescope (Klotz et al. 2009) from $T_0 + 492$ s up to $T_0 + 3.7$ ks (Klotz et al. 2011). A successful Target of Opportunity (ToO) was performed with *XMM-Newton* (Gendre et al. 2011) for a total exposure time of 51.5 ks between $T_0 + 56.7$ ks and $T_0 + 108.2$ ks. This GRB was also detected with *Konus-WIND* (KW) at $T_0 - 1900$ s and showed evidence of a weaker emission from $T_0 - 5400$ s to $T_0 - 2600$ s (Golenetskii et al. 2011). Light curves from KW have been publicly released in the GRB Coordinates Network Circular and are accessible through the web.⁹

We refer the reader to Paper I for the methods of data reduction from *Swift*/XRT, as well as from *XMM-Newton*. To convert the KW counts into flux density we first computed the background-subtracted total counts from the digitalized light curve in the 20–1400 keV energy range during the main burst, that is, from $T_0 - 1990$ s to $T_0 + 4400$ s, where we know the fluence to be $(4.86 \pm 0.61) \times 10^{-4}$ erg cm⁻² in the energy range of 20 keV < E < 1400 keV (Golenetskii et al. 2011). By assuming the claimed best-fit spectral model, that is, a cut-off power-law model $dN/dE \propto (E/\Gamma_{\text{KW}}) e^{-E(2+\Gamma_{\text{KW}})/E_{\text{cut}}}$ with a best-fit photon index of $\Gamma_{\text{KW}} = -1.31 \pm 0.09$ and cut-off energy of $E_{\text{cut}} = 310 \pm 53$ keV, we were able to estimate the flux density at the mean energy of the 20–1400 keV photon spectrum, that is, at ~ 116 keV.

NIR and optical afterglow data from the GROND telescope, as well as from the Gemini and Very Large Telescope (VLT) telescopes, have been taken from Kann et al. (2011a) and from Levan et al. (2013) and corrected for the Galactic extinction $E(B - V) = 0.02$ mag in the direction of the burst (Schlegel et al. 1998). Radio fluxes of GRB 111209A simultaneously measured with the Australia Telescope Compact Array (ATCA) in two bands, 5.5 and 9 GHz, at the mean observing time of 11:12 UT, that is, at $T_0 + 446.4$ ks or $T_0 + 5.2$ days (~ 3.5 days after optical rebrightening peak), have been taken from Hancock et al. (2011).

The resulting multiwavelength light curve of GRB 111209A is plotted in Figure 1.

2.1. *Swift*/BAT Data Reduction

To build the *Swift*/BAT 15–150 keV flux density light curve, we converted fluxes taken from the light curve repository¹⁰ (Evans et al. 2009, 2010) into flux densities. We assumed a power-law spectral model and used the available time resolved photon index estimates. We computed the flux density at the energy of ~ 47 keV, that is at the mean energy of the 15–150 keV average photon spectrum (Palmer et al. 2011).

We also extracted the energy spectra at two epochs where simultaneous UVOT and XRT data were available in order to perform multiband analysis. To this end, data (obsid 00509337 000) were reduced following the standard procedure described in the BAT data analysis threads.¹¹ In order to estimate the proper geometric parameters for making an accurate response matrix, we used the task *batmaskwtevt* to build the missing auxiliary raytracing file, where we adopted the optical *Swift*/UVOT source coordinates R.A. = 14.34429 deg and Decl. = -46.80106 deg (Hoversten et al. 2011b).

2.2. *Swift*/UVOT Data Reduction

The optical counterpart of GRB 111209A was detected in all seven UVOT filters. Observations were taken in both image and event modes. Before extracting count rates from the event lists, the astrometry was refined following the methodology described in Oates et al. (2009). For both the event and image mode data, the source counts were extracted using a region of 5'' or 3'' radius. As it is more accurate to use smaller source apertures when the count rate is low (Poole et al. 2008), the 3'' aperture was used when the count rate fell below 0.5 counts s⁻¹. In order to be consistent with the UVOT calibration, these count rates were then corrected to 5'' using the curve of growth contained in the calibration files. Background counts were extracted using a circular region of radius 20'' from a blank area of sky situated near the source position. The count rates were obtained from the event and image lists using the *Swift* tools *uvotevt1c* and *uvotsource*, respectively. They were converted to magnitudes using the UVOT photometric zero points (Breeveld et al. 2011). The analysis pipeline used software HEADAS 6.10 and UVOT calibration 20130118.

2.3. TAROT Data Reduction

Exposure of the field of GRB 111209A with the TAROT ESO (Chile) robotic telescope (Klotz et al. 2009) was taken with the tracking speed adapted to obtain a small 10 pixel trail. This technique was used in order to obtain continuous temporal information during the exposure (Klotz et al. 2006). The spatial sampling was 3''.29 pixel⁻¹, and the FWHM of stars (in the perpendicular direction of the trail) was 2.05 pixels. Only the first exposure was performed with this technique. Successive images were tracked on the diurnal motion using exposure times increasing from 30 s to 180 s.

Images were not filtered. We used the star NOMAD-1 0431-0011481 ($R = 11.56$, $V - R = +0.34$) as a constant template for calibration for all TAROT images. We used the AudeLA software¹² to compute the magnitude using a point-spread function fit with the template star. The fit leads to the optical flux ratio GRB/template which is converted into *R* magnitudes. Results are quoted in Table 1.

⁹ <http://www.ioffe.rssi.ru/LEA/GRBs/GRB111209A>

¹⁰ http://www.swift.ac.uk/burst_analyser/

¹¹ <http://heasarc.nasa.gov/docs/Swift/analysis/>

¹² <http://www.audela.org/>

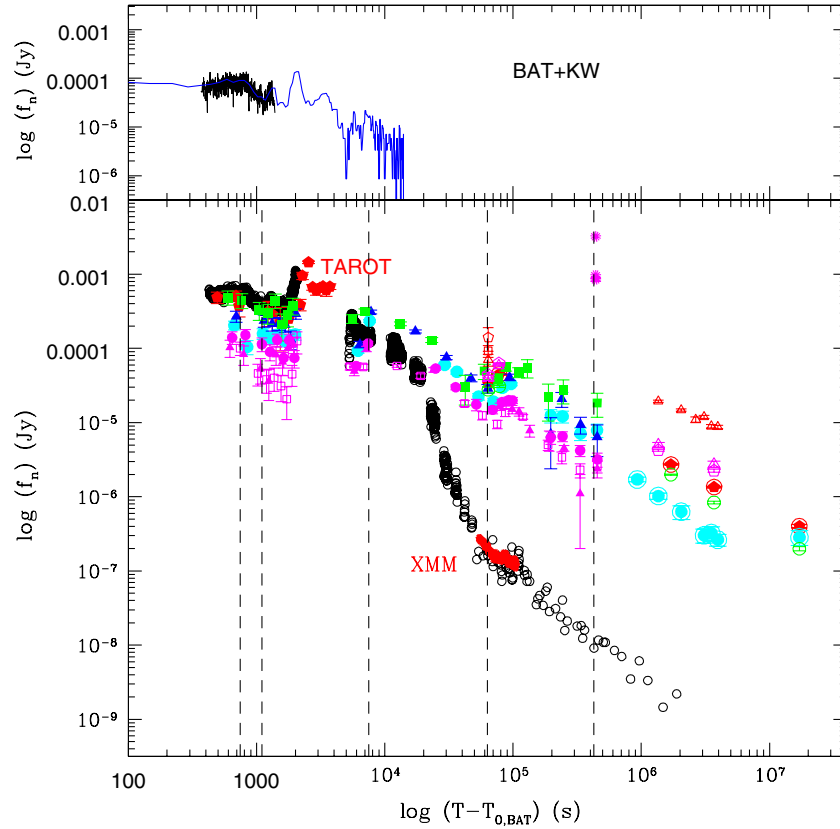


Figure 1. Multiwavelength light curve of GRB 111209A. Top panel: *Swift*/BAT (black) and *Konus-WIND* (blue). Bottom panel: *Swift*/XRT (black open circles), *XMM* (red starred circles), TAROT (red-filled pentagons), *Swift*/UVOT: *w*2-band (magenta open squares), *m*2-band (magenta-filled triangles), *w*1-band (magenta-filled circles), *u*-band (cyan-filled circles), *b*-band (blue-filled triangles), *v*-band (green-filled squares), and ground-based telescopes from Levan et al. (2013) and GCN Circulars: *u*-band (cyan dotted circles), *g*-band (green open circles), *r*-band (red encircled pentagons), *i*-band (magenta open triangles), *z*-band (magenta open pentagons), *J*-band (red open triangles), *H*-band (red open squares), *K*-band (red open pentagons), and radio-band (magenta stars). The vertical dashed lines indicate the central epochs at which we extract radio/optical to X-ray spectral energy distribution (see text): 650–850, 1–1.2 ks, and 7–8 ks (prompt emission); 62–64 ks (GROND data epoch); and 426–466 ks after the trigger (radio data epoch).

(A color version of this figure is available in the online journal.)

Table 1
TAROT *R*-band Observations (See Section 2.3)

T_{start} (min)	T_{stop} (min)	Flux (mJy)	mag AB	dmag AB
7.95	8.45	0.4875	17.18	0.21
11.20	11.70	0.5105	17.13	0.20
11.87	12.37	0.3733	17.47	0.27
19.61	21.11	0.3133	17.66	0.29
21.28	22.78	0.2884	17.75	0.33
24.62	26.12	0.2249	18.02	0.33
28.86	30.36	0.2512	17.90	0.28
35.53	37.03	0.3873	17.43	0.17
37.20	38.70	0.955	16.45	0.26
40.80	43.80	1.445	16.00	0.13
43.96	46.96	0.6668	16.84	0.15
47.13	50.13	0.6026	16.95	0.21
50.30	53.30	0.6546	16.86	0.21
53.46	56.46	0.6855	16.81	0.15
56.63	59.63	0.6138	16.93	0.27
60.61	63.61	0.6792	16.82	0.15
1037.91	1311.70	0.0198	20.66	0.10

Note. Flux and apparent magnitudes are not corrected for Galactic extinction.

3. THE PROMPT EMISSION

In this section we analyze the prompt emission temporal and spectral properties by using simultaneous optical, X-ray, and gamma-ray data.

3.1. The Optical Flare Temporal Lag

In Figure 2 we plot a light curve comparison in each energy band for the time interval $T_0 - 3000$ s to $T_0 + 8000$ s, where T_0 refers to the first BAT trigger time (see Section 2). Between $\sim T_0 + 400$ s and $\sim T_0 + 4000$ s, the prompt emission of GRB 111209A was observed in a large frequency window, that is, from optical wavelengths to gamma-rays.

A pronounced flare is observed in the KW data at $\sim T_0 + 2$ ks and is clearly visible at all wavelengths, although a complete monitoring before and after the flare peak epoch was possible only with the TAROT *R*-band and KW data. Assuming a Gaussian, we measure a peak epoch at (2460 ± 50) s after T_0 and a width of ~ 130 s using the TAROT data; using KW data we measure a peak epoch at (2050 ± 10) s after T_0 and a width consistent with the optical one. The delay of the *R* band peak epoch is thus 410 ± 50 s with respect to the gamma-ray peak epoch, that is, ~ 245 s in the rest frame of the burst.

We discuss some possible origins of this temporal lag in Section 5.3.

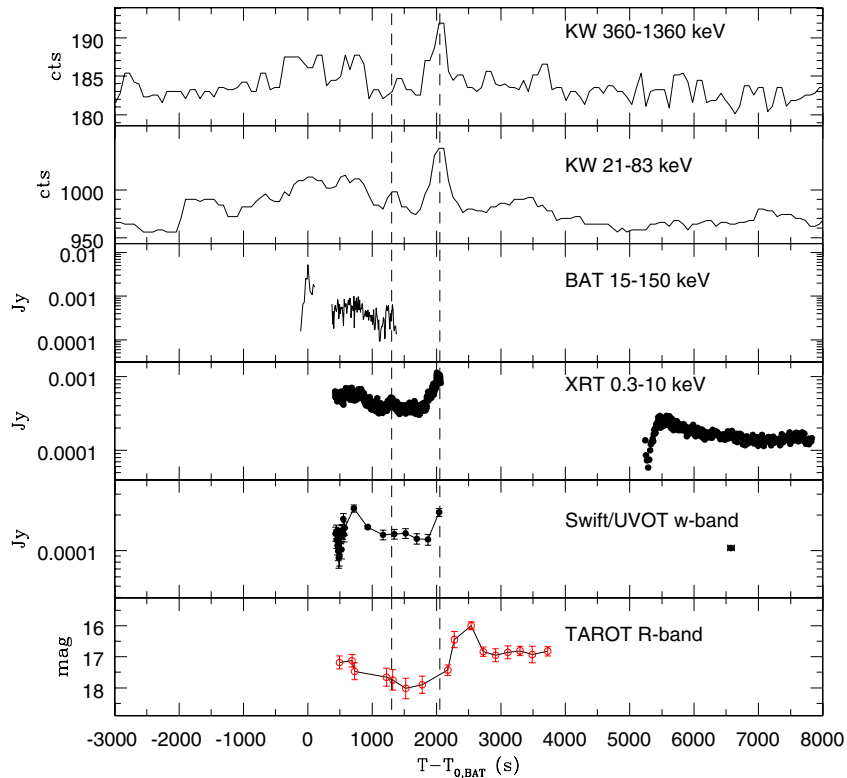


Figure 2. Prompt emission light curve between -3000 and 8000 s from the BAT trigger, at different wavelengths. Vertical dashed lines indicate the peak of two high energy flares computed at $T_0 + 1.3$ ks from *Swift*/XRT data analysis and at $T_0 + 2.0$ ks from *Konus-WIND* light data analysis.

(A color version of this figure is available in the online journal.)

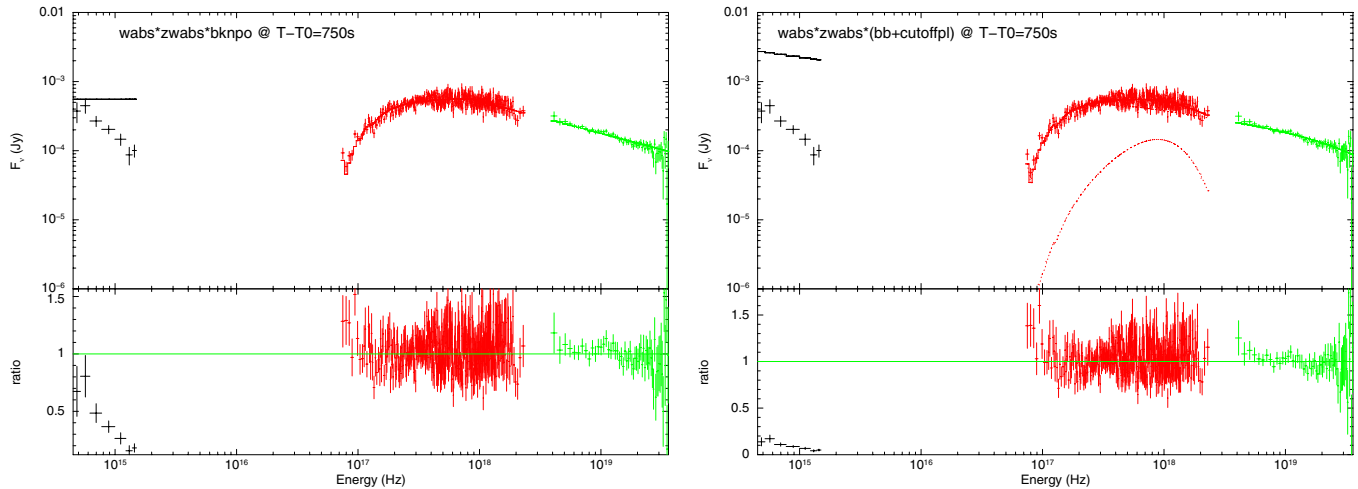


Figure 3. Prompt emission X-ray to optical SED centered at 750 s after the trigger where simultaneous TAROT (*R* band) and *Swift*/UVOT *v*, *b*, *u*, *w1*, *m2*, *w2* bands (black); XRT 0.3–10 keV (red); and 15–150 keV BAT (green) data are available. The black lines are the best fit continuum obtained from the simultaneous fit of the BAT and XRT data by assuming a broken power-law model and a cut-off power-law model plus a black-body component. The optical fluxes are systematically below the model and can be fit assuming a significant dust extinction. In Table 2 we quote the results obtained by including the optical data in the fit.

(A color version of this figure is available in the online journal.)

3.2. The Prompt SED

The quasi-simultaneous optical and gamma-rays flaring activity at $\sim T_0 + 2$ ks (Section 3.1) may suggest a common origin of the emission mechanism responsible for the optical and high-energy radiation. We further investigate this hypothesis by analyzing the simultaneous optical to X-ray spectral energy distribution (SED). To this end, we extract the *Swift*/UVOT, XRT, and BAT data energy spectrum in three temporal intervals. We select the ranges 650–850 s and 1–1.2 ks after T_0 , as they were

covered in a large frequency window and free of flaring activity (Figure 1). In addition, we extract a third SED at 7–8 ks after T_0 where only *Swift*/UVOT and XRT energy spectra were available.

To begin, we simultaneously fit the XRT and BAT data assuming a broken power law and a Band spectral model. As clearly shown in Figure 3 for the broken power-law case, while the 15–150 keV spectrum is consistent with the extrapolation from the 0.3–10 keV spectrum to higher energies, the simultaneous TAROT and *Swift*/UVOT *R*, *v*, *b*, *u*, *w1*, *m2*, and

Table 2
Multiband Prompt Spectral Analysis at Three Different Epochs

$T - T_0$ (ks)	β_1	β_2	E_0 (keV)	$N_{H,z}$ (10^{21} cm^{-2})	$E(B - V)$ (mag)	T (keV)	$\chi^2(\text{dof})$	$\chi^2_{\text{noBB}}(\text{dof})$	$F\text{-test}$ $p\text{-value}$
BPL+BB									
0.65–0.85	0.0 ± 0.1	0.47 ± 0.02	$3.7^{+0.8}_{-0.4}$	3.3 ± 0.4	0.17 ± 0.03	$0.04^{+0.02}_{-0.01}$	483(446)	501(448)	3e-4
1–1.2	0.1 ± 0.1	0.57 ± 0.02	2.7 ± 0.2	2.5 ± 0.2	0.24 ± 0.03	0.04 ± 0.01	401(414)	420(416)	7e-5
7–8	-0.7 ± 0.6	0.7 ± 0.2	$0.02^{+0.60}_{-0.01}$	2.9 ± 0.2	0.22 ± 0.03	1.25 ± 0.2	262(288)	283(290)	1e-5
Band+BB									
0.65–0.85	0.0 ± 0.1	0.49 ± 0.02	16^{+7}_{-4}	3.7 ± 0.4	0.14 ± 0.03	0.05 ± 0.01	473(466)	498(448)	3e-4
1–1.2	0.0 ± 0.1	0.59 ± 0.02	9 ± 2	3.0 ± 0.3	0.23 ± 0.03	0.04 ± 0.01	393(414)	422(416)	4e-7
7–8	0.11 ± 0.03	1.7 ± 0.2	$1.8^{+0.9}_{-0.5}$	2.4 ± 0.2	0.26 ± 0.03	1.25 ± 0.2	273(288)	286(290)	1e-3
CPL+BB									
0.65–0.85	0.25 ± 0.01	...	≤ 257	2.9 ± 0.3	0.35 ± 0.02	1.3 ± 0.1	512(447)	698(449)	8e-31
1–1.2	0.36 ± 0.01	...	≤ 257	2.4 ± 0.3	0.47 ± 0.03	1.0 ± 0.1	433(415)	623(417)	2e-33
7–8	0.41 ± 0.03	...	≤ 257	1.8 ± 0.2	0.32 ± 0.03	0.3 ± 0.1	382(289)	422(291)	6e-7

Notes. Best-fit parameters for each spectral model are quoted in three rows. The first and second rows refer to the periods 650–850 s and 1000–1200 s after T_0 where simultaneous TAROT, *Swift*/UVOT, *Swift*/XRT, and *Swift*/BAT were available. The third row refers to the period 7–8 ks after T_0 where *Swift*/XRT and UVOT data were available. Three different spectral continuum were assumed (BPL = broken power law, Band = Band model, CPL = cut-off power law) along with a blackbody component (BB). The χ^2 of the same fit without the BB component is also quoted (χ^2_{noBB}) as its statistical significance which is computed through an F -test. The optical dust reddening was estimated in the rest frame of the burst and is best fit with a SMC-like extinction curve, except for the CPL model during the first two epochs for which a MW extinction law better fit the data.

w2 SED provides a measured softer spectrum, with spectral index $\beta_{\text{opt}} = 1.43 \pm 0.20$, which at odds with the expectations where both X-rays and optical emission is synchrotron radiation from the same population of electrons with a power-law SED. Indeed, for synchrotron models, the spectral slope always gets steeper (thus softer) with increasing frequency.

In analogy with the study of the prompt emission spectral continuum of other LGRBs (e.g., GRB 100901A, Gorboskoy et al. 2012), a non-negligible absorption by dust in the host galaxy allows us to recover the optical with the X-ray spectrum. We test this hypothesis by simultaneously fitting BAT, XRT, UVOT, and TAROT data¹³ and by assuming three possible dust extinction laws (the Galactic and the two Magellanic Clouds ones) using the software XSPEC (Arnaud 1996) v12.8.0. We find acceptable solutions, which are listed in Table 2. Assuming a Band model rather than a broken power-law model does not significantly improve the goodness of the fit. In both cases (Band and broken power-law model), we find that the Small Magellanic Cloud dust extinction curve best fit the data, as opposed to the Milky Way (MW) and Large Magellanic Cloud (LMC) laws. In addition, for both spectral continuum models, the fit improves with the addition of a black-body component in the soft X–far UV energy range, which is consistent with the spectral analysis results obtained from fitting the XRT data only (published in Paper I). In Table 2 we quote the statistical significance of the fit improvements with the addition of a black-body spectral component.

From the KW data spectrum integrated over the main burst, that is, from $T_0 - 1990$ to $T_0 + 4400$ s, we learn that the best-fit spectral model in the 20–1400 keV energy range is a cut-off power law with a spectral index of $\beta_{\text{KW}} = 0.31 \pm 0.09$ (photon index $\Gamma_{\text{KW}} = -1.31$) and a cut-off energy of $E_{\text{cut}} = 310 \pm 53$ keV (Golenetskii et al. 2011). This model is in agreement with the well known $E_{\text{iso}} - E_{\text{peak}}$ correlation (Amati et al. 2002, 2010), according to which the expected νF_ν peak energy value is about a few hundreds of keV given the large equivalent isotropic energy value for this burst of $E_{\text{iso}} = (5.7 \pm 0.7) \times 10^{53}$ erg

(Golenetskii et al. 2011). Therefore, by assuming that the bulk of the radiation for this burst is emitted at energies above the BAT energy range (i.e., $E_{\text{peak}} > 150(1+z)$ keV), we test the KW exponential cut-off power-law model on the simultaneous *Swift*/XRT and BAT spectrum by fixing the photon index and cut-off energy to vary within their uncertainties, that is, with a cut-off energy in the range 257–363 keV and a spectral index in the range of 0.22–0.44, and allowing the normalization to vary. The best-fit model can reproduce our estimate of the KW flux density at 2.8×10^{19} Hz (i.e., 116 keV; see Section 2), that is, $\sim 9 \times 10^{-5}$ Jy at $T - T_0 = 650\text{--}850$ s and $\sim 4 \times 10^{-5}$ Jy at $T - T_0 = 1\text{--}1.2$ ks, but could only marginally fit the XRT and BAT data ($\chi^2/\text{dof} = 676/443$). By introducing a blackbody component we find a significant improvement of the fit ($\chi^2/\text{dof} = 500/441$) with $kT \sim 1$ keV. By assuming two blackbody components, we find further improvement to the fit with the second thermal component in the FUV energy range ($\chi^2/\text{dof} = 466/439$).

Also in this case, however, the optical fluxes are severely underpredicted by this model (Figure 3). Given the harder photon index inferred from the cut-off power-law model, the extrapolation to the optical range requires a larger amount of dust extinction. In addition, a different dust extinction law, more similar to the MW law rather than the SMC law, seems to better represent the observations.

Therefore, regardless of the assumed intrinsic spectral model, we find that the optical emission is consistent with the X-ray/gamma-ray spectral continuum only if a non-negligible amount of dust is introduced.

3.3. Dust to Gas Ratio

A considerable amount of dust along the line of sight should be reflected in the X-ray data analysis with a certain amount of equivalent hydrogen (gas) column. Past studies have shown that, on average, the N_H/A_V measured ratio in optically bright GRBs is about 10 times higher than expected in a Milky-Way- or Magellanic-Cloud-like environments (e.g., Galama & Wijers 2001; Stratta et al. 2004; Kann et al. 2006; Schady et al. 2010), although with a large scatter.

¹³ We used the `f1x2xsp` tool to build the optical flux spectrum.

Table 3
Swift/UVOT Best Fit Parameters of the Light Curves in the Temporal Interval 3–1000 ks by Assuming Two Broken Power Laws (Where Each Power Law Segment is Represented by $F(t) \propto t^{-\alpha}$)

Band	α_1	t_b (ks)	α_2	$\alpha_{r,1}$	$t_{b,r}$ (ks)	$\alpha_{r,2}$
<i>u</i>	~ -4.2	~ 10	~ 2.0	~ -3.3	92 ± 5	1.1 ± 0.2
<i>b</i>	~ -4.4	~ 9	~ 1.5	~ -2.9	~ 131	2.3 ± 0.3
<i>v</i>	~ -0.9	8 ± 1	1.2 ± 0.2	~ -1.4	113 ± 10	0.7 ± 0.4
<i>w</i>	-0.5 ± 0.1	14.8 ± 0.5	1.6 ± 0.1	~ -3.1	104	$1.3^{+0.2}_{-0.6}$
Mean	-0.5 ± 0.1	13.4 ± 0.4	1.5 ± 0.1	-2.0 ± 0.5	96 ± 4	1.3 ± 0.1
<i>v</i> -norm	-0.35 ± 0.10	15.5 ± 0.4	1.6 ± 0.1	-2.0 ± 0.5	102 ± 2	1.3 ± 0.1

Notes. The “on-set bump” rising and decay indices, as well as its peak epoch, are α_1 , α_2 , and t_b . The suffix “r” indicates the same parameters for the late rebrightening feature. The row “mean” quotes the weighted mean of each parameter measured in the optical range for values that we could not compute uncertainties due to poor statistics, we considered a relative uncertainty of 50%. The row “*v*-norm” quotes the results obtained from the light curve obtained with all filters, normalized to the *v*-band fluxes (see the text).

The average value of $\langle N_H/A_V \rangle = (3.3 \pm 2.8) \times 10^{22} \text{ cm}^{-2} \text{ mag}^{-1}$ has been measured for a sample of optically bright GRBs assuming a SMC environment (Schady et al. 2010). Assuming an MW extinction curve, the typical GRB average $\langle N_H/A_V \rangle$ is $(2.1 \pm 1.8) \times 10^{22} \text{ cm}^{-2} \text{ mag}^{-1}$ (Schady et al. 2010). From the measured N_H obtained during prompt emission analysis of GRB 111209A (Table 2), we can estimate an expected range of dust extinction values of $A_{V,\text{exp}} = N_H/\langle N_H/A_V \rangle = [0.04\text{--}0.8] \text{ mag}$ for an SMC environment and $[0.05\text{--}1] \text{ mag}$ for an MW environment. Assuming a broken power law and a Band model, these values encompass the measured $A_V = R_V \times E(B - V)$ that we find in the range $\sim 0.3\text{--}0.85 \text{ mag}$. Indeed, for these models we find a best fit for a SMC dust extinction law that requires a total-to-selective extinction parameter R_V of 2.93 (Pei 1992).

By assuming a cut-off power-law spectral model for the prompt spectral continuum, the extrapolation up to the optical range requires an MW-like extinction law with A_V values estimated in the range of 0.9–1.5 mag for $R_V = 3.1$ (Pei 1992). These values are consistent only with the highest values of the expected A_V range. More consistent values are obtained if we assume the empirical N_H/A_V ratio measured in our Galaxy, that is, $\langle N_H/A_V \rangle_{\text{MW}} = 1.8 \times 10^{21} \text{ cm}^{-2} \text{ mag}^{-1}$ (Predehl & Schmitt 1995).

Given the better consistency of a cut-off power-law model with both the KW data analysis (Golenetskii et al. 2011) and the expected $E_{\text{iso}}\text{--}E_{\text{peak}}$ correlation for LGRBs, we tentatively conclude that a dust-to-gas ratio similar to that one observed in our Galaxy is preferred for GRB 111209A.

4. THE AFTERGLOW EMISSION

In this section we analyze the prompt to afterglow transition and the afterglow properties through a multiwavelength data analysis. We assume the standard paradigm in which the steep decay phase observed in X-rays is evidence of high latitude emission from the prompt phase (Kumar & Panaitescu 2000), while the following shallow decay observed in the *XMM-Newton* data and the normal decay observed in the *Swift*/XRT data, represent the afterglow emission.

4.1. *Swift*/UVOT Optical Light Curve and Spectral Analysis

Starting from the second *Swift* orbit after the trigger, that is, from $\sim T_0 + 3 \text{ ks}$, the optical flux shows a marginal increase at all wavelengths up to about 10 ks after the trigger. This may suggest

that a different emission component is emerging over the end part of the prompt emission. This phase is then followed by a smooth power-law decay up to about 1 day after T_0 . Another rebrightening is then observed to peak around $T_0 + 1.16 \text{ days}$ (e.g., Figure 1; see also Kann & Greiner 2011b).

In order to better quantify this behavior, we fit the light curves extracted in each UVOT filter. We assume a model formed by the sum of two broken power laws, in the temporal range that goes from $T_0 + 3 \text{ ks}$ to $T_0 + 1 \text{ Ms}$ ($\sim 10 \text{ days}$). To have a prompt comparison with the X-ray light curve, we plot the latter in the same figure. Not all the model parameters could be quantified by fitting the light curve extracted in each separate UVOT filter. Therefore, to increase the available statistics and better define the model parameters, we normalize all fluxes to the *v*-band flux following Oates et al. (2009), i.e., using data between 20 ks and 70 ks, under the assumption that spectral variability is not significant across the light curve. This assumption is supported by the fact that no spectral dependence of α_2 is detected (see Table 3). We then grouped the resulting light curve with a time resolution of $\delta t/t \sim 0.1$. Results for the *u*, *b*, *v*, and *white* filters, as well as for the coadded and *v*-band normalized light curves, are quoted in Table 3 and plotted in Figure 4, together with the X-ray light curve (top panel).

The rising flux behavior around 5–10 ks for the *v*-band normalized optical light curve is very steep, and has a power law index of -3.7 ± 0.3 ; it is preceded by marginal evidence of a rapid flux decay with an index ~ 1 . Considering that at this time the gamma-ray emission is still active, this result may indicate a possible contamination from a non-negligible optical flaring activity, preventing a careful analysis of the optical rising phase and of the peak epoch estimate. On the other hand, after $\sim T_0 + 10 \text{ ks}$ the decay slope shows a more smoothed behavior at all wavelengths within the uncertainties. Results are quoted in Table 3.

We then extract the spectral information at several epochs. The latter epochs were selected in order to minimize the uncertainties introduced by the necessary temporal extrapolation at each specific epoch of the sparse data sample. We apply a smooth polynomial function to approximate the light curve in each band, and then we compute the average value for each selected temporal interval and for each filter. Using *Swift*/UVOT data, we measure an energy spectral index of $\beta_{\text{opt}} = 1.60 \pm 0.25$ and $\beta_{\text{opt}} = 1.33 \pm 0.01$, respectively, between 7 and 8 ks, and between 20 and 40 ks after T_0 . We note that at a redshift $z = 0.677$ the UVOT frequencies trace the rest frame UV

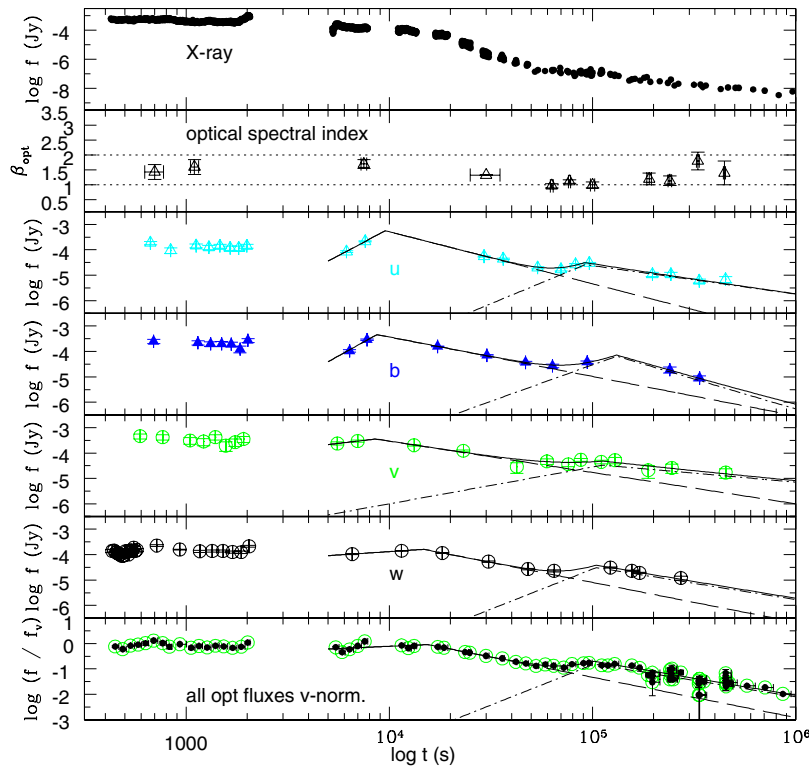


Figure 4. *Swift*/UVOT white, u, b, and v filter light curves, as well as the *Swift*/UVOT co added light curve normalized to the v-band (bottom panel), compared with the *Swift*/XRT light curve (top panel) and the optical spectral indices versus time from trigger. All the light curves have been fitted in the temporal range 3–1000 ks from the BAT trigger by the sum (continuous line) of two broken power laws (long dashed line and dot-dashed line).

(A color version of this figure is available in the online journal.)

emitted radiation, but given the large sensibility of this energy range to even small amount of dust along the line of sight, the true spectral slope may be harder than the measured value.

In contrast, just before the rebrightening we were able to measure the spectral index also using NIR data taken with the GROND telescope at $T_0 + 63$ ks (Figure 5). The resulting optical/NIR SED is well-fitted by a simple power law with a spectral index of $\beta_{\text{opt}} = 1.07 \pm 0.15$. Another epoch where we were able to exploit simultaneous NIR data is around 77 ks, where VLT g, R, i and z data are available in addition to the *Swift*/UVOT; here we measure $\beta_{\text{opt}} = 1.11 \pm 0.06$.

Around the rebrightening peak, between 90 and 100 ks after T_0 , the optical/UV spectral index is $\beta_{\text{opt}} = 1.0 \pm 0.1$. After the peak, the optical/UV spectral slopes soften significantly. We were able to measure the optical spectral index at four postbrightening epochs where *Swift*/UVOT data were taken nearly simultaneous in all filters. We find $\beta_{\text{opt}} = 1.2 \pm 0.2$ at $T_0 + 190$ ks, $\beta_{\text{opt}} = 1.14 \pm 0.16$ at $T_0 + 240$ ks, $\beta_{\text{opt}} = 1.8 \pm 0.3$ at $T_0 + 330$ ks, and $\beta_{\text{opt}} = 1.4 \pm 0.4$ at $T_0 + 446$ ks, that is, at the radio epoch data (see Section 4.3).

An early “bump” and a late rebrightening have been observed in several “normally” LGRBs. Liang et al. (2013) provide an extensive data analysis of these optical features for a large sample of 146 optically monitored LGRBs. In 38 and 27 GRBs, on-set bumps and rebrightenings have been detected, respectively. In 12 cases both features were present in each optical light curve. The rising index distribution of the on-set features ranges from -0.3 to -4 with a mean of about -1.5 , and it is consistent with the rising index distribution of the late rebrightening. The decay indices distribution of both the on-set bumps and late rebrightenings ranges within 0.6 – 1.8 , with a mean of 1.15 , apart from three outliers with a decay index greater

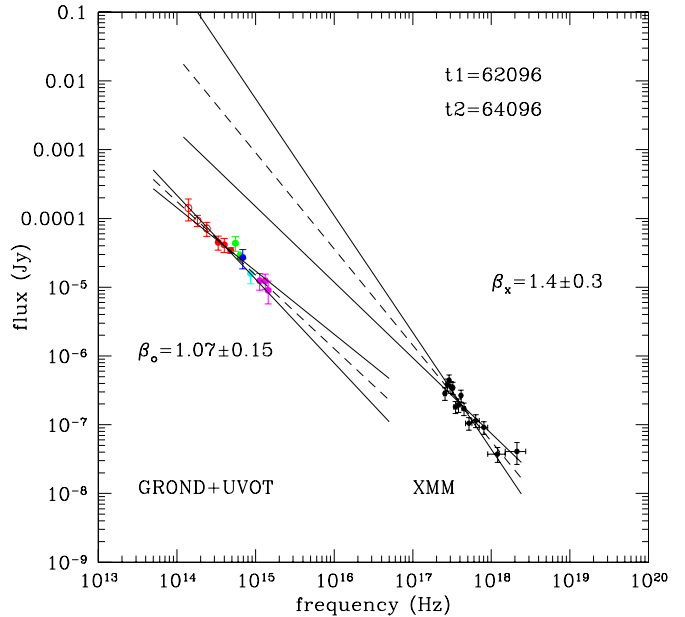


Figure 5. Spectral energy distribution at the GROND data epoch at $T_0 + 63$ ks (17 hr after the trigger), where the *grizJHK* GROND data are plotted together with the simultaneous *Swift*/UVOT and XMM data.

(A color version of this figure is available in the online journal.)

than 2. The on-set optical bump peak epoch usually coincides with the X-ray light curve entering in the steep decay phase, suggesting a different origin of the radiation observed in the two energy domains at that time, while late optical rebrightenings are on average also tracked in X-rays.

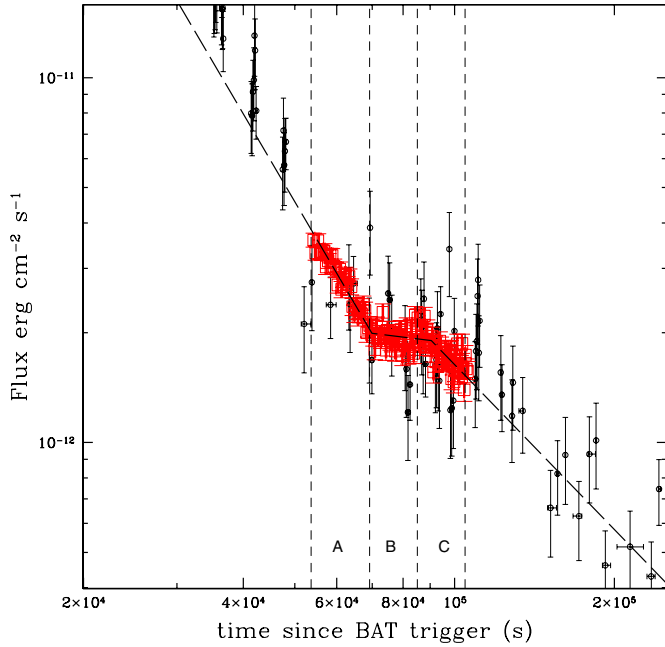


Figure 6. *Swift*/XRT PC (black open circles) and the *XMM-Newton* PN (red open squares) X-ray flux light curve. The dashed line is the best fit obtained from simultaneous *XMM-Newton* and *Swift*/XRT PC data.

(A color version of this figure is available in the online journal.)

We find that the optical afterglow of GRB 111209A fits with the average behavior; the only marked difference is in the peak time of the on-set bump. Indeed, while the late rebrightening peak epoch is consistent with the poorly defined typical range that goes from several hundreds of seconds to days after the burst trigger, the on-set bump of GRB 111209A at $T_0 + 10$ ks peaks at much later times than the typical 30–3000 s on-set peak epoch after the burst trigger time. These findings support our impression that the prompt emission contamination is indeed preventing us from making the correct estimate of the rising index and the peak epoch of the early optical emission. We discuss some possible interpretations of the optical afterglow feature origin in Section 5.5

4.2. The Late Afterglow as Observed by *XMM-Newton*

The exceptionally high quality of *XMM* data enabled us to detect the presence of a plateau at the end of the steep decay with more statistical confidence than using *Swift*/XRT data alone. Assuming a broken power-law model, we find an initial steep decay index of $\alpha_{1,XMM} = 2.23 \pm 0.10$ and a break at $t_{b,1} = 70 \pm 1$ ks followed by a shallower decay with an index of $\alpha_{2,XMM} = 0.53 \pm 0.05$. This model could only marginally reproduce the data ($\chi^2 = 143/100$). By extrapolating this model at late times, it clearly overpredicts the ending part of the *XMM-Newton* data as well as the following *Swift*/XRT PC fluxes. A significant χ^2 improvement was obtained by allowing the presence of a second temporal break at $t_{b,2} = 87 \pm 1$ ks ($\chi^2 = 124/98$). Performing an *F*-test to evaluate the statistical significance of the addition of a second temporal break, we find a null-hypothesis probability value (*P*-value) of 0.001. A simultaneous fit of the *XMM-Newton* data and the *Swift*/XRT PC data from $T_0 + 100$ ks up to the *Swift*/XRT monitoring end ($T_0 + 2$ Ms) provides a better constraint of the final decay slope, with $\alpha_{3,XMM+XRT} = 1.52 \pm 0.06$ and a shallow decay phase with $\alpha_{2,XMM+XRT} = 0.18 \pm 0.05$ (Figure 6).

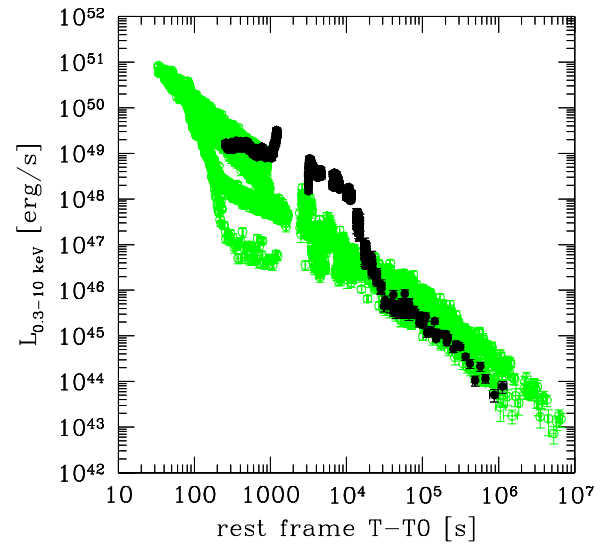


Figure 7. X-ray (0.3–10 keV) rest-frame luminosity of GRB 111209A (black) and of a sample of LGRBs at known redshift that are consistent with the ICG model (green) taken from Pisani et al. (2013).

(A color version of this figure is available in the online journal.)

Shallow decay phases, or plateaus, are commonly observed in GRB X-ray light curves with *Swift*/XRT (Liang et al. 2010). A characteristic property of X-ray plateaus is that the X-ray luminosity at the end of the plateau typically scales with the rest-frame epoch of the plateau end as $L_X \sim 10^{51} T_{\text{end}}^{-1} \text{ erg s}^{-1}$, although with a large scatter (Dainotti et al. 2010). For GRB 111209A, we measure $L_X \sim 4 \times 10^{45} \text{ erg s}^{-1}$ at the rest-frame epoch of the plateau $T_{\text{end}} = t_{b,2}/(1+z) \sim 52$ ks after T_0 (Figure 7). These values make GRB 111209A marginally consistent with the correlation within its large intrinsic scatter and put it at the bottom-right end of the L_X – T_{end} plane where there are GRBs with the faintest and longest plateaus.

We divided the *XMM* observations into three temporal bins tracking the “steep-flat-steep” phases, labeled as “A,” “B,” and “C” in Figure 6. We then fitted the X-ray spectra integrated in each bin with a simple and a double power-law model. Results are quoted in Table 4. Uncertainties are at a 90% confidence level. The resulting 0.3–12.0 keV PN energy spectrum and the two 0.2–10.0 keV MOS spectra, all grouped in order to have at least 20 counts per energy bin and fitted simultaneously, are plotted in Figure 8. During the first (A) and only marginally on the second (B) temporal bin, data are better fitted by the addition of a second harder component to the standard power-law soft spectrum usually detected during this phase with *Swift*/XRT data. Performing an *F*-test, the statistical significance of the additional hard power-law is measured with a null hypothesis probability of 10^{-8} and 10^{-4} during bins A and B, respectively (Table 4). We discuss the possible origins of this component in Section 5.

4.3. The Late Radio to X-Ray Afterglow SED

Nearly simultaneous radio, X-rays, and optical data in the *w2*, *m2*, *w1*, *u*, *b*, and *v* filters are available at $T_0 + 5.2$ days. We corrected the optical flux from Galactic absorption and plot them together with the unabsorbed X-ray and radio data (Figure 9). The X-ray spectrum was extracted in the temporal range that goes from $T_0 + 250$ ks to $T_0 + 650$ ks using the *Swift*/XRT spectra repository time-sliced spectral analysis tool. The X-ray spectral index of $\beta_X = 1.8 \pm 0.4$ and the decay index of $\alpha_X = 1.5 \pm 0.1$

Table 4
XMM Data Spectral Analysis

Bin	Time Range (ks)	Model	β_1	β_2	$N_{H,z}$ (10^{21} cm^{-2})	$\chi^2(\text{dof})$	$F_1(F_{1,\text{unabs}})$ (0.3–12 keV)	$F_2(F_{2,\text{unabs}})$ (10^{-12} cgs)	F-test
A	56.7–70.0	PL	1.30 ± 0.05	...	1.6 ± 0.2	650(604)	2.2(2.7)
B	70.0–87.7	PL	1.40 ± 0.06	...	1.5 ± 0.2	583(537)	1.4(1.9)
C	87.7–108.2	PL	1.4 ± 0.1	...	1.8 ± 0.2	600(586)	1.3(1.8)
A	56.7–70.0	2PL	$1.7^{+0.8}_{-0.3}$	$0.3^{+0.6}_{-1.0}$	$2.4^{+0.4}_{-0.7}$	615(602)	1.5(2.5)	0.9(0.9)	6e-8
B	70.0–87.7	2PL	$1.6^{+0.7}_{-0.2}$	$0.0^{+2.3}_{-1.3}$	$2.0^{+0.6}_{-0.3}$	565(535)	1.2(1.8)	0.3(0.3)	2e-4
C	87.7–108.2	2PL	$1.6^{+2.0}_{-0.1}$	$-0.1^{+3.7}_{-3.1}$	$2.0^{+3.2}_{-0.3}$	595(584)	1.2(1.8)	0.2(0.2)	0.1

are consistent with the synchrotron model expectations for $\nu_X > \nu_c$, where ν_c is the cooling frequency of the electrons (Sari et al. 1998). By fixing the optical spectral index to be free to vary within β_X and $\beta_X - 0.5$ (including the uncertainties on β_X), the optical to X-ray data are best fit by a broken power-law model with $\beta_X = 1.6 \pm 0.4$, $\beta_{\text{opt}} = 0.87 \pm 0.03$, a break energy in the range 0.6–1.4 keV, and no rest frame visual dust extinction ($\chi^2 = 10.5$ for 10 degrees of freedom). Despite the large uncertainty affecting the X-ray spectral slope, a simple power-law spectral continuum between the X-rays and the optical frequencies provides a much worse fit ($\chi^2 = 19$ for 12 degrees of freedom). Thus, we can confidently exclude this model. Radio data alone provide excellent agreement with the expected one-third spectral slope if ν_{radio} were below the spectral peak frequency. Following Panaitescu & Kumar (2000), we were able to fit the multiband SED for $\nu_{\text{radio}} < \nu_m < \nu_{\text{opt}} < \nu_c < \nu_X$, where ν_m is the synchrotron injection frequency (Sari et al. 1998), with the following parameters: an environment density of $n = 0.07 \text{ cm}^{-3}$, a fraction of the total energy transferred to the magnetic field of $\epsilon_B = 0.0003$ and to the swept-up electrons of $\epsilon_e = 0.03$, an electron power-law energy distribution index of $p = 2.6$, an energy conversion efficiency of $\eta = 0.1$, a collimation factor of 0.08 (i.e., a half-opening angle of 23°). We could not find any obvious solution that assumes a wind environment.

5. DISCUSSION

5.1. Evidence of Dust Destruction?

We have seen in Section 3.2 that by interpreting the prompt optical emission observed by *Swift*/UVOT and TAROT as originating from the same physical mechanism responsible for the observed emission in X-rays and gamma-rays, we are forced to declare a non-negligible amount of dust.

While invoking dust extinction is not rare in the afterglow spectral analysis, given our ignorance of the physical radiative mechanism of the prompt emission, the possibility that a distinct phenomenology is mimicked by dust extinction cannot be excluded. In particular, for GRB 111209A we have seen that at about $T_0 + 2$ ks a flare that is clearly detected with TAROT and KW shows an optical peak epoch delayed by about 400 s from the gamma-ray peak. If all of the optical emission is delayed with respect to the high-energy counterpart, the simultaneous prompt emission SED should take into account such temporal lag. We test this scenario by simultaneously fitting X-ray spectrum extracted at $T_0 + 700$ s with optical spectrum at $T_0 + 1100$ s, but even in this case, we find that the optical fluxes are severely underestimated and a non-negligible dust extinction may recover the expected values. Another way a dust extinction effect is mimicked is with the presence of a spectral break

between the X-rays and the optical energy domains. However, we have already considered this case in our heuristic broken power-law spectral model with a break energy in or below the soft X-ray energy range, and we have shown that the much softer optical spectral index can recover the expected harder optical to X-ray spectral slope with the presence of dust extinction.

Interestingly, non-negligible dust extinction during the prompt emission has already been invoked for another very long GRB whose duration falls near the right end of the burst duration distribution, that is, GRB 100901A with $T_{90} = 439 \pm 33$ s (Sakamoto et al. 2010). In that case, in order to match the optical data with the X-ray extrapolation during the prompt emission where simultaneous optical to gamma-ray spectra were available, a rest-frame visual dust extinction of $A_V \sim 0.6$ –1.6 was introduced (Gorbovskey et al. 2012). In addition, two dark GRBs with $A_V > 5$ mag in the rest frame were found to have a very long duration prompt emission, with $T_{90} \sim 800$ s, although other LGRBs with $T_{90} > 500$ s were found with no evidence of strong dust extinction (Zauderer et al. 2013).

However, for GRB 111209A, we find that gathering evidence of dust extinction from the afterglow emission is more contrived. The best measure we could perform of any dust reddening in the afterglow emission was obtained at $T_0 + 63$ ks when simultaneous GROND and *Swift*/UVOT data were available and provided a NIR-to-UV SED. We could not find any evidence of large dust extinction effects because they are well fit by a simple power-law model ($\chi^2 = 9.5$ with 10 degrees of freedom), with a 90% upper limit of $A_V < 0.3$ mag. In Figure 5 we plot the simultaneous NIR/optical and X-ray spectra. Despite the fact that spectral slopes in the two energy regimes are consistent within their uncertainties, there is a clear normalization mismatch. This is not surprising as at this epoch the X-ray emission is likely still affected by the prompt emission.¹⁴ Even while neglecting any prompt contribution, we find that the two spectra can be modeled with a broken power-law ($\chi^2/\text{d.o.f.} = 19/15$), with a 2σ upper limit of $A_V < 0.15$. At $T_0 + 77$ ks simultaneous SEDs using *XMM-Newton* and UVOT data, as well as VLT *g*, *r*, *i* and *z* observations from Levan et al. (2013), were available. Again, we find similar results, with a rest-frame dust extinction of $A_V < 0.1$ mag.

From the gas column measured using *XMM-Newton* data in the rest frame of the burst, we find the range of values 1 – $4 \times 10^{21} \text{ cm}^{-2}$ (Table 4) by assuming a solar abundance and a cold environment. These values provide an expected dust extinction $A_{V,\text{exp}}$ of the order of ≤ 0.1 mag assuming the average GRB $\langle N_H/A_V \rangle = (2.1 \pm 1.8) \times 10^{22}$ for a MW environment

¹⁴ Note that the X-ray spectrum plotted in Figure 5 is integrated over the small temporal interval $t_2 - t_1$ around the GROND observation epoch, and collected photons provide insufficient statistics to detect the hard component (see Section 4.2).

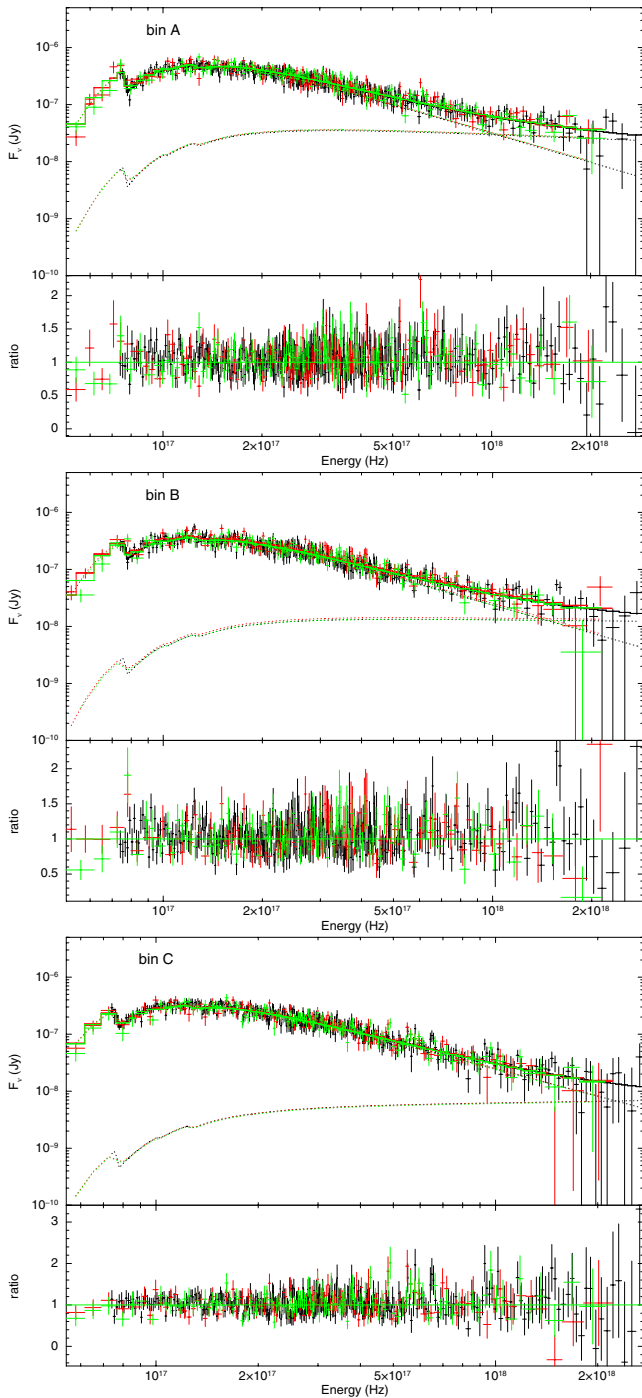


Figure 8. *XMM* PN and MOS 1 and 2 spectra extracted at three different epochs (during the steep phase, the plateau phase, and after the end of the plateau phase), fitted with two absorbed power laws. The three temporal bins are marked as A, B, and C in Figure 6. Best-fit parameters are quoted in Table 4.

(A color version of this figure is available in the online journal.)

(Schady et al. 2010) or an $A_{V,\text{exp}} = [0.6\text{--}2.2]$ mag assuming the empirical N_H/A_V observed in our Galaxy. Finally, from the radio-to-X-ray SED extracted at 443 ks after T_0 , we find no evidence of dust extinction.

The low-dust extinction level inferred from the optical afterglow analysis, as well as the contrasts with the prompt emission findings and with the expected A_V from the *XMM-Newton* data analysis, can be reconciliated by assuming that an effective dust destruction mechanism is at play during the prompt and the afterglow emission. In this case, the dust inferred during the

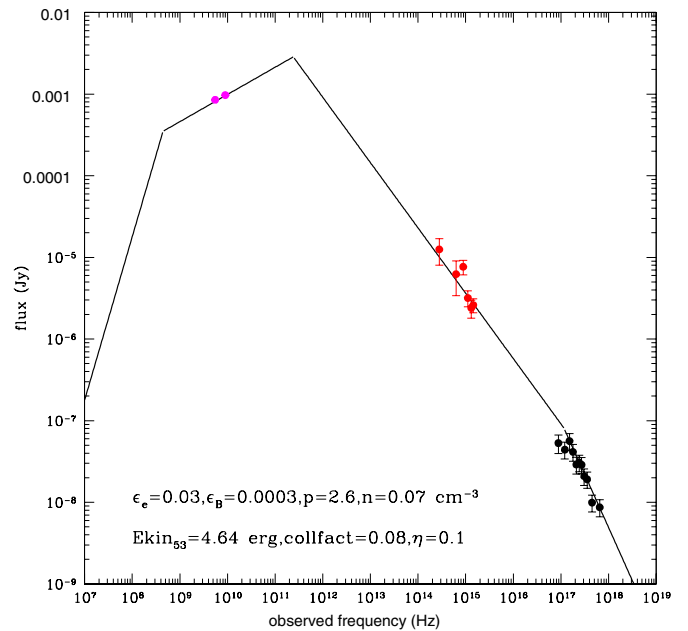


Figure 9. Simultaneous radio (magenta-filled points); *Swift*/UVOT *m*2, *w*1, *u*, *v*; and *Swift*/XRT X-ray data spectral energy distribution at the epoch of radio observations (around five days after the trigger). The solid line is the solution found in the context of the synchrotron emission model following Panaitescu & Kumar (2000).

(A color version of this figure is available in the online journal.)

prompt emission should be located not too distant from the central engine. Dust destruction simulations show that intense GRB fluxes can destroy dust up to a radius of ~ 10 pc (e.g., Waxman & Draine 2000), consistent with a dense and dusty star forming region in which the GRB is embedded, although the possibility that the dust is produced by the progenitor star itself cannot be excluded. Dust destruction is a likely possibility given the intense UV and soft X-ray photon fluxes from a GRB, and possible evidence of such a mechanism has been recently suggested for GRB 120119 during the final phases of the prompt emission (Morgan et al. 2013), which is exactly as we propose the case to be for GRB 111209A.

5.2. Implications for the BSG Progenitor

The presence of dust in the host galaxy of GRB 111209A is in line with the recent findings of a subsolar, but not especially low host galaxy metallicity. From the host galaxy spectroscopy it has been found a metallicity $12 + \log(\text{O}/\text{H}) = 8.3 \pm 0.3$ (Levan et al. 2013) and assuming $\log(Z/Z_\odot) = 12 + \log(\text{O}/\text{H}) - 8.76$ (Caffau et al. 2008), we infer $\sim 0.35 Z_\odot$. At the same time, because host metallicity likely reflects the star metallicity for short-lived sources such as massive stars, this result is at odds with a Blue Supergiant (BSG) progenitor interpretation (Gendre et al. 2013; Nakauchi et al. 2013). Indeed, following Woosley & Heger (2012), a low-metallicity condition of $< 0.1 Z_\odot$ was invoked for this progenitor star (Paper I) in order to prevent strong wind and thus to provide sufficient mass to supply the central engine over several hours.

A possible solution can be found in a binary system formation channel of the blue supergiant (e.g., Podsiadlowski 1992). Binary systems, either formed by two massive stars or a massive star and a low-mass companion (Fryer & Heger 2005; Podsiadlowski et al. 2010), have been invoked to deal with the increasing evidence that a large fraction of LGRBs explode in high-metallicity environments, that is, where the required high

core angular momentum condition is expected to be suppressed by strong winds (see a recent review by e.g., Levesque 2013, and reference therein). A binary system that comprises a Helium star and a NS within a common envelope phase (Fryer & Woosley 1998) has been suggested for GRB 101225A, another ultra-long burst (with bursts duration >2000 s) that shares similar host galaxy properties with GRB 111209A (Levan et al. 2013) but for which a clear thermal component was detected in the optical afterglow between one and several tens of days after the trigger (Thöene et al. 2011), contrary to what we see for GRB 111209A.

Another interesting scenario suggested by a binary system progenitor for LGRBs is the Induced Gravitational Collapse (IGC) of a NS into a black hole (BH) through accretion from a massive companion during its SN phase (Ruffini et al. 2001). This scenario could explain a number of LGRBs with burst durations (T_{90}) in the range ~ 10 – 100 s, as well as their afterglow phenomenology (Izzo et al. 2012; Pennacchioni et al. 2012, 2013). The IGC model predicts a number of features: a precursor in the prompt emission light curve due to the initial phase of the SN, an optical SN Ic signature tens of days after the burst onset, and a universal rest frame 0.3–10 keV light curve at late times (Pisani et al. 2013), possibly due to the newly born NS after the SN phase of the donor star. Whether this model applies to the ultra-long GRB 111209A requires accurate modeling. However, the KW light curve of GRB 111209A clearly shows a precursor¹⁵ at about $\sim T_0 - 10$ ks. The detection of a SN for GRB 111209A is not obvious from the late-time optical light curve, although possible indirect evidence has been discussed by Levan et al. (2013). Finally, by comparing the sample of IGC-GRBs at known redshift (Pisani et al. 2013) with GRB 111209A, we find that the late X-ray afterglow luminosity of GRB 111209A shows a consistent behavior starting from about $T - T_0 = 30$ ks in the rest frame (Figure 7). Following Pisani et al. (2013), we further make a blind search of the redshift by comparing the expected GRB 111209A X-ray luminosities if the burst were at redshift $z = 0.4, 0.5, 0.6, 0.7$, and 0.8 , with the prototype light curve of GRB 090618; we find that residuals are minimized for a redshift between 0.6 and 0.7 , which is consistent with the spectroscopic redshift of $z = 0.677$ of GRB 111209A.

5.3. The Optical Temporal Lag: Evidence of Two Emitting Regions?

Though optical flare lags have been already observed in other LGRBs, the lag measured for GRB 111209A of ~ 245 s in the rest frame is far larger than what was reported earlier. For example, for GRB 081126 at redshift $2.8 < z < 3.8$ and with burst duration of $T_{90} \sim 55$ s, a temporal lag of (8.4 ± 3.9) s was measured for a prompt emission flare (Klotz et al. 2009). For XRF 071031 at $z = 2.692$ and with $T_{90} \sim 180$ s an optical flare lag was measured to be 35 s in the burst frame (Kruhler et al. 2009). No temporal lag was found for a simultaneous prompt emission optical and gamma-ray flare detected in two very long GRB 110205A at $z = 2.22$ (Gendre et al. 2012) and GRB 100901A at $z = 1.408$ (Gorbovskoy et al. 2012), with $T_{90} = 260$ s and $T_{90} = 439$ s, respectively. A 2 s delay was observed between the gamma-ray and optical variable emission during the prompt emission of the very bright “naked eye” burst GRB 080319B at $z = 0.937$ with $T_{90} > 50$ s (e.g., Beskin et al. 2010). All these temporal lags range below ~ 50 s in the burst rest frame, and there is no obvious connection with the

burst duration that would explain the much longer delay of the ultra-long GRB 111209A.

In general, flares observed in X-rays and gamma-rays are known to show faster rising, faster decaying profiles, as well as earlier peaks at high energies rather than at low energies due to a hard-to-soft spectral evolution (e.g., Margutti et al. 2011). The optical lags observed in some GRBs may be an extension of this property in the optical energy domain. The large diversity on the optical temporal gaps observed among several LGRBs may be due to different dynamics of the synchrotron frequencies crossing the two energy domains (e.g., Kruhler 2011).

In the framework of the internal shock model, another possible explanation of the optical temporal lag predicts that the optical counterpart of the gamma-ray flare is generated by synchrotron mechanism in a different, optically thin region of the ejecta, more distant from the inner, optically thick regions where gamma rays are generated. To reproduce two distinct emitting regions, one possible scenario is based on the assumption of a large neutron ejecta component: delayed flare optical counterpart can originate during the time when a late ejected proton shell catches up with an earlier ejected neutron shell that has traveled far away from the central engine with negligible interactions with the ejecta, where electrons are produced through neutron β -decay (Fan et al. 2009). The predicted time delay between the optical and gamma-ray peaks is expected to be of the order of 2–3 s for $\Gamma \sim 300$ (from $\Delta t \sim 1.1(1+z)300/\Gamma$ s, Fan et al. 2009); thus it can reproduce the large temporal lag observed for GRB 111209A only for a neutron shell Lorentz factor of a few. In an alternative scenario, a delayed optical emission can originate from “residual” collisions at larger distance R from the central engine (Li & Waxman 2008). Temporal delay of the order of a fraction of a few seconds is obtained for fiducial values of $R \sim 10^{15}$ cm and $\Gamma \sim 300$ from $\Delta t \sim R/2c\Gamma^2$. Large time delays such as those observed in GRB 111209A, for which $R \sim 1.5 \times 10^{13} \Gamma^2$ cm, could thus be achieved assuming low Γ values or large radii.

5.4. The X-Ray Hard Extra Power Law Component Origin

In Section 4.2 the temporally resolved spectral analysis of the *XMM-Newton* data suggests the presence of two spectral components at the end of the steep decay phase, where the hardest component dominates at high energies (see β_1 and β_2 in Table 4 and Figure 8). An intriguing explanation of the hard spectral component in the *XMM-Newton* spectrum can be found following the recent gamma-ray instruments findings in the GRB observational campaigns. Some bursts observed by *Fermi* in the Large Area Telescope (LAT) energy range (20 MeV–300 GeV), for instance GRB 090902B (Abdo et al. 2009), show the presence of a very hard power-law spectral component in addition to the typical prompt emission spectrum that is usually fitted by a Band law or a cut-off power law.

The power-law extracomponent is present during the prompt phase. It decays once the afterglow has started (e.g., Abdo et al. 2009) and is very hard (e.g., an energy spectral index of $\beta_h = 0.62 \pm 0.03$ for GRB 090510, Ackermann et al. 2010). One may thus consider the extracomponent seen in GRB 111209A as the “soft tail” of this hard power-law seen by the *Fermi*/LAT. The fact that we detect it only at the end of the steep decay phase is linked to its properties: the hard power-law component intensity rises slowly during the prompt phase and is typically detected when the X-ray prompt emission has just ended. At this point it decays following a power law (see, e.g., Zhang et al. 2011 for a review). In our case, the soft tail of

¹⁵ <http://www.ioffe.rssi.ru/LEA/GRBs/GRB111209A>

this component is too faint to be detected during the prompt emission while it emerges when the main X-ray prompt spectral continuum drops down to small flux levels at the end of the steep decay phase. By modeling the temporal evolution of the hard component (see F_2 values in the temporal bins A, B, and C in Table 4) with a power-law decay, we were able to roughly measure a decay index of $\alpha_h = 3.8^{+1.2}_{-3.0}$ that, despite the large uncertainties, is consistent with past measures (e.g., ~ 0.8 in the case of GRB 090902B, ~ 1.1 for GRB 090510; see Ackermann et al. 2013). Also, it may be steeper than the afterglow decay that, at that epoch, is entering in the shallow decay phase, thus preventing further detections at later times of the hard component.

Ironically, one of the two GRBs for which the prompt extraspectral component has been unambiguously detected (GRB 090902B and GRB 090510) is a short GRB, that is, at the opposite end of the burst duration distribution range from the ultra-long GRB 111209A. The extra power-law spectral feature was also detected for GRB 090510, for which the burst duration was ~ 20 s.

Zhang et al. (2011) denote this extra power-law as “Component III,” in addition to the Band model (“Component I”) and a thermal component (“Component II”). Among the possible interpretations of Component III (see Zhang et al. 2011 and references therein) has been the proposal that it may originate from the Compton-upscattered emission of a simultaneous thermal emission in the MeV energy range (“Component II”) that was observed in both GRB 090510 and 090902B. Although we detect a thermal emission for GRB 111209A, it was in the soft X-ray energy range and not simultaneous to the power-law extracomponent. An alternative scenario suggests that “Component III” is emitted from another site using the classical emission mechanism for GRBs (Zhang et al. 2011). As discussed in Section 5.3, a scenario involving two different emission sites could stand for GRB 111209A.

5.5. The Origin of the Optical Afterglow Emission

In the following section, we attempt to interpret the origin of the early and late optical afterglow emission in the paradigm of the fireball model.

For the early afterglow, given the large uncertainties affecting the rising phase of the optical on-set bump, we consider here only its decaying properties. We have seen that between 20 and 40 ks, the flux decays following a power law with an average index of $\alpha_2 = 1.6 \pm 0.1$ (Table 3). In the same temporal interval, we measure a spectral index of $\beta_{\text{opt}} = 1.33 \pm 0.01$ using *Swift*/UVOT data (Section 4.1). In the following, we explore three possible scenarios of this early emission.

Forward shock. According to the synchrotron closure relationships between the temporal and spectral indices, the expected spectral slope during this phase is $\beta = 2\alpha/3 = 1.1 \pm 0.1$ or $\beta = (2\alpha + 1)/3 = 1.4 \pm 0.1$ for $\nu_m < \nu < \nu_c$ or $\nu > \nu_c$, respectively, where ν_c is the synchrotron cooling frequency and ν_m is the frequency at which the bulk of the electrons are radiating (Sari et al. 1998). The measured spectral index β_{opt} is thus consistent within the uncertainties with the case $\nu_{\text{opt}} > \nu_c$. Alternatively, the case $\nu_{\text{opt}} < \nu_c$ may also be valid assuming a certain amount of dust extinction.¹⁶

If forward shock (FS) is the correct interpretation, the bump at $T_0 + 10$ ks marks the fireball deceleration epoch. Assuming a constant density environment in the range $n = 0.01\text{--}1\text{ cm}^{-3}$ and an energy conversion efficiency of $\eta = 0.1\text{--}0.2$, we find an initial Lorentz factor Γ_0 value of the order of $\sim 50\text{--}120$ and a deceleration radius of $\sim 4\text{--}20 \times 10^{17}$ cm by simply equating the fireball energy with the swept-up mass energy assuming a spherical geometry (Sari et al. 1998). The lack of evidence of a further steepening of the light curve before ~ 50 ks, that is before the epoch when the rebrightening phase starts to dominate, imposes a lower limit to the jet opening angle. Assuming a range of density values between 0.01 and 1 cm^{-3} , we estimate that the jet half opening angle should be larger than $\sim 1^\circ\text{--}4^\circ$.¹⁷

Reverse shock. An alternative interpretation of the early optical decay can be found in the reverse shock (RS), formed in the fireball impact with the surrounding medium. Indeed, RS emission is expected to produce early optical “flashes” peaking at epochs comparable to the burst duration (Kobayashi et al. 2000). This may be the case for the early optical emission of GRB 111209A, the decaying behavior of which starts roughly at the estimated end of the prompt emission, as expected. Given the ultra-long duration of the burst, it is likely that the so-called “thick shell” case applies for GRB 111209A. In the “thick shell” case, the RS has enough time to accelerate to relativistic velocities within the shell. Like the forward shock case, the expected spectral behavior of the RS follows the synchrotron emission prescriptions. According to Kobayashi et al. (2000), for $\nu_{\text{opt}} < \nu_c$, a flux decay is expected to have a power-law index of $\alpha = (73p + 21)/96$, which is consistent with the measured decay index α_2 (Table 3) for an electron (power-law) energy distribution index of $p \sim 1.8$. We note that from the late afterglow radio-to-X-ray SED we infer a higher value of p (see Section 4.3). Thus, if the RS is the correct interpretation, these results possibly indicate an evolution of the microphysical parameters between the early and the late afterglow phases.

For $\nu_{\text{opt}} > \nu_c$, the RS emission rises to a constant flux phase up to the end of the prompt duration; it then vanishes as no electrons are shocked after the RS has crossed the shell. Thus, if $\nu_{\text{opt}} > \nu_c$, the RS scenario cannot explain the observed smooth flux decay.

Internal shock. Another possible interpretation associates the steep optical decay with the high-latitude emission from the internal shocks emission (IS) formed within the ejecta and also responsible for the X-ray and gamma-ray emission. However, in this case, the predicted decay rate is $\alpha = (2 + \beta) \geq 3$ (e.g., Kumar & Panaitescu 2000), which is much steeper than the measured rate. Thus, we can exclude this scenario. In addition, the radius where IS takes place is typically smaller than the external shock; this makes an IS decay time scale in the order of several tens of kiloseconds unlikely (e.g., Wu et al. 2013).

We will now interpret the rebrightening observed at $T_0 + 100$ ks. Before the rebrightening peak, the estimated mean rising index is $\alpha_{r,1} = -2.0 \pm 0.5$ (Table 3), while the spectral index is $\beta_{\text{opt}} = 1.0 \pm 0.1$ up to the rebrightening peak epoch (measured from NIR and optical data, Section 4.1). The X-ray plateau is observed nearly simultaneously with the optical

¹⁶ We have considered the case of a slow-cooling regime of the bulk of the electrons. In the case of fast cooling, the two expected spectral indices are associated to the following frequency ranges $\nu_c < \nu < \nu_m$ and $\nu > \nu_m$ (Sari et al. 1998)

¹⁷ We caution that the rebrightening at ~ 1 day after the trigger may indicate, among several scenarios, an energy injection or the emergence of an additional jet component. Therefore, assuming the initial kinetic energy and the lower limit of the jet break time to estimate the jet opening angle of GRB 111209A may be an oversimplification.

rebrightening. Several hypothesis have been made to interpret the late rebrightening observed in many LGRBs.

Structured jet model. A rebrightening feature can be reproduced by a two-jet component scenario. One possible configuration predicts that the prompt and the early afterglow emission are produced by a fast, narrow jet, while the late rebrightening is due to the deceleration process of a wide, slower jet that may dominate the emission from the other jet at late times (e.g., Peng et al. 2005). We have already seen that the early optical afterglow emission of GRB 111209A can be interpreted in the context of the FS emission; in this scenario, the FS is formed in the impact between the narrow jet with the interstellar medium (ISM). However, if the rebrightening were produced by the FS of the wider jet, according to the FS modeling (Sari et al. 1998), we would expect a slower rising index and a much harder spectrum than what we are able to measure during the rising phase. In addition, we do not find marked evidence of spectral evolution near the peak epoch as expected from the crossing of the injection synchrotron frequency.

An alternative scenario assumes that the two jets have different axis orientations with respect to the line of sight of the observer, where the off-axis jet originates the rebrightening as an effect of the jet approaching the line of sight (e.g., Huang et al. 2004). In this scenario, a large variety of rising behaviors can be reproduced depending on the angle formed between the line of sight and the jet axis. In this case, in order to dominate the on-axis jet emission at late times, the off-axis jet component should be more energetic. For GRB 111209A, for which $E_{\text{iso}} \geq 10^{53}$ erg (e.g., Golenetskii et al. 2011), the latter condition makes this scenario not favorable, although it cannot be excluded.

Late-prompt model. A large range of possible rebrightening morphologies can also be reproduced by the so-called “late-prompt model” (e.g., Ghisellini et al. 2007). In this model, the rebrightening feature is the emerging of the prolonged central engine emission from the decaying afterglow signal. However, this model predicts a strong spectral evolution during the rebrightening that is not so evident for GRB 111209A (Figure 4).

Density gradient. One possibility invokes a density gradient in the circumburst environment if the condition $v < v_c$ is satisfied (e.g., Lazzati et al. 2002). Since the first studies on this hypothesis, the vast phenomenology observed so far has shown that additional requirements should be included in the density gradient scenario in order to reproduce the observations. In particular, Kong et al. (2010) were able to reproduce a large variety of late rebrightening morphologies by allowing the shock microphysics parameters to vary between an initial wind environment and the following shocked constant density environment.

Delayed energy injection. Another possible interpretation of the late rebrightening is associated with a late energy injection given by the delayed interaction of slow ejected shells with the fireball (e.g., Fan & Piran 2006). This model has been frequently invoked to explain the X-ray shallow phase observed in a large fraction of X-ray afterglows soon after the steep decay phase. Energy injection models do not predict any spectral variability; indeed, during the plateau in X-rays of GRB 111209A, we could detect the presence of a spectral component with a nearly constant spectral slope $\beta_X = 1.7 \pm 0.1$ (Table 4). In this scenario, the late optical rebrightening is simply the optical counterpart of the X-ray emission, unless assuming that it is by chance simultaneous with the X-ray plateau.

6. SUMMARY AND CONCLUSIONS

We have analyzed the extensive multiwavelength data set of the “ultra-long” GRB 111209A from the prompt emission to the late afterglow. During the prompt emission, at 2 ks from T_0 , we measure an unprecedented large temporal lag of ~ 245 s in the burst rest-frame between the optical and the high energy peak time of a pronounced flare. This lag may be evidence of two distinct emission regions for the gamma-rays and optical observed radiation, although other scenarios cannot be excluded.

Separate emission regions may also be supported by evidence of an extra hard power-law component in the X-ray spectrum at the end of the prompt emission if it is interpreted as the soft tail of the hard power-law component observed in few cases by gamma-ray instruments at the prompt-to-afterglow transition phase (e.g., Zhang et al. 2011).

Assuming a common origin of the optical and high energy prompt photons, a non-negligible amount of dust extinction should be invoked, in analogy with some other very long GRBs for which simultaneous optical-to-gamma-ray prompt emission data were available (e.g., GRB 100901A Gorbovskoy et al. (2012)) and with two very dark GRBs with prompt durations of about 800 s (Zauderer et al. 2013). The afterglow data analysis, however, does not confirm the presence of dust, possibly indicating that the intense UV and X-ray flux from the GRB have partially destroyed the dust along the line of sight in the host galaxy.

The presence of dust is consistent with the findings of a subsolar, but not exceptionally low, metallicity in the host galaxy of GRB 111209A and is at odds with the very low metallicity environment invoked for a blue supergiant progenitor (see Paper I). A possible solution can be found by invoking a binary system formation channel of the blue supergiant, as proposed by Podsiadlowski (1992). The evolution of a binary system of two massive stars or a massive star and a small mass companion has often been invoked for LGRBs in order to confront the increasing evidence of a significant fraction of LGRBs in high metal-content host galaxies (see, e.g., Levesque 2013 for a recent review). In addition, binary systems are at the basis of the IGC model that provides a unified view of the phenomenology observed in both the prompt and the afterglow of some LGRBs (Ruffini et al. 2001).

Despite the exceptional longevity of GRB 111209A, its afterglow is not dissimilar from other normally LGRBs in terms of optical and X-ray afterglow light curves and spectra. Indeed, the prompt-to-afterglow transition in both X-rays and optical wavelengths does not differ from several other LGRBs studied in the past that show an initial flux decay with different decay indices in the two energy ranges, followed by an optical rebrightening nearly simultaneous to an X-ray plateau.

The spectral and temporal information available during the early optical afterglow decay prevents us from discerning between a forward shock or a RS origin, but it enables us to exclude an internal shock origin. In the FS case, a Lorentz factor of ~ 50 – 120 and a deceleration radius of ~ 4 – 5×10^{17} cm are inferred.

The late afterglow tentatively favors the presence of a prolonged energy injection from the central engine that, if true, should be active up to 70–80 ks after the trigger, that is, for a dozen hours in the rest frame. However, the late rebrightening can also be explained through (1) a density gradient, as expected in the likely complex environment surrounding the progenitor of GRB 111209A or (2) by a structured jet scenario. The

radio—to—X-ray broad band SED at 5 days after the trigger is consistent with the synchrotron model for a fireball expanding in an ISM with a density of $\sim 0.1 \text{ cm}^{-3}$ and a predicted large half-opening angle of the jet ($\sim 23^\circ$).

Finally, we note that the existence of a bright optical emission associated with an ultra-long GRB with a flux level above 0.1–1 mJy up to several hours after the trigger may increase the orphan afterglow detection probability, a still unresolved fundamental issue that would definitively provide access to the jetted nature of these events (e.g., Atteia 2013).

We thank the anonymous referee for useful comments and suggestions that have led to an overall improvement of the manuscript. We also thank D. A. Kann for useful discussion. This work made use of data supplied by the UK *Swift* Science Data Centre at the University of Leicester and is a result of the FIGARO collaboration. It was supported by the French Programme National des Hautes Energies and by the ASI grant I/009/10/0. We acknowledge the use of public data from the *Swift* data archive. TAROT has been built with the support of the CNRS-INSU. Finally, we thank the technical support of the *XMM-Newton* staff, in particular N. Loiseau and N. Scharrel. S.O. and M.D.P. acknowledge funding from the UK Space Agency.

Facilities: Swift, XMM, TAROT-Calern, TAROT-ESO

REFERENCES

- Abdo, A. A., Ackermann, M., Ajello, M., et al. 2009, *ApJL*, **706**, L138
- Ackermann, M., Ajello, M., Asano, K., et al. 2013, *ApJS*, **209**, 11
- Ackermann, M., Asano, K., Atwood, W. B., et al. 2010, *ApJ*, **716**, 1187
- Amati, L., Fronter, F., & Guidorzi, C. 2010, *A&A*, **508**, 173
- Amati, L., Frontera, F., Tavani, M., et al. 2002, *A&A*, **390**, 81
- Arnaud, K. A. 1996, in ASP Conf. Ser. 101, *Astronomical Data Analysis Software and Systems V*, ed. G. H. Jacoby & J. Barnes (San Francisco, CA: ASP), 17
- Atteia, J. L. 2013, in Proc. of 9th INTEGRAL Workshop and Celebration of the 10th Anniversary of the Launch, *An INTEGRAL View of the High-energy Sky* (Paris: Bibliotheque Nationale de France), <http://pos.sissa.it/cgi-bin/reader/conf.cgi?confid=176>
- Beskin, G., Karpov, S., Bondar, S., et al. 2010, *ApJL*, **719**, L10
- Breeveld, A. A., Landsman, W., Holland, S. T., et al. 2011, in AIP Conf. Ser. 1358, *Gamma Ray Bursts 2010* (Melville, NY: AIP), 373
- Caffau, E., Sbordone, L., Ludwig, H.-G., et al. 2008, *A&A*, **483**, 591
- Dainotti, M. G., Willingale, R., Capozziello, S., Fabrizio Cardone, V., & Ostrowski, M. 2010, *ApJL*, **722**, L215
- Evans, P., Beardmore, A. P., Page, K. L., et al. 2009, *MNRAS*, **397**, 1177
- Evans, P., Willingale, R., Osborne, J. P., et al. 2010, *A&A*, **519**, 102
- Fan, Y., & Piran, T. 2006, *MNRAS*, **369**, 197
- Fan, Y., Zhang, B., & Wei, D. 2009, *PhRv*, **79**, 021301
- Fryer, C. L., & Heger, A. 2005, *ApJ*, **623**, 302
- Fryer, C. L., & Woosley, S. E. 1998, *ApJL*, **502**, L9
- Galama, T. J., & Wijers, R. A. M. J. 2001, *ApJ*, **549**, 209
- Gendre, B., Atteia, J. L., Boer, M., et al. 2011, GCN Circular, 12638
- Gendre, B., Atteia, J. L., Boer, M., et al. 2012, *ApJ*, **748**, 59
- Gendre, B., Stratta, G., Atteia, J.-L., et al. 2013, *ApJ*, **766**, 30
- Ghisellini, G., Ghirlanda, G., Nava, L., & Firmani, C. 2007, *ApJL*, **658**, L75
- Golenetskii, S., Aptekar, R., Mazets, E., et al. 2011, GCN Circular, 12663
- Gorbovskey, E. S., Lipunova, G. V., Lipunov, V. M., et al. 2012, *MNRAS*, **421**, 1874
- Hancock, P. J., Tara, M., Bryan, G., & Zauderer, A. 2011, GCN Circular, 12804
- Hoversten, E. A., Burrows, D. N., Campana, S., et al. 2011b, GCN Circular, 12641
- Hoversten, E. A., Evans, P. A., Guidorzi, C., et al. 2011a, GCN Circular, 12632
- Huang, Y. F., Wu, X. F., Dai, Z. G., Ma, H. T., & Lu, T. 2004, *ApJ*, **605**, 300
- Izzo, L., Ruffini, R., Penacchioni, A. V., et al. 2012, *A&A*, **543**, 10
- Kann, D. A., & Greiner, J. 2011b, GCN Circular, 12656
- Kann, D. A., Klose, S., Kruehler, T., & Greiner, J. 2011a, GCN Circular, 12647
- Kann, D. A., Klose, S., & Zeh, A. 2006, *ApJ*, **641**, 993
- Kashiyama, K., Nakauchi, D., Suwa, Y., et al. 2013, *ApJ*, **770**, 8
- Klotz, A., Gendre, B., Atteia, J.-L., et al. 2009, *ApJ*, **697**, 18
- Klotz, A., Gendre, B., Boer, M., & Atteia, J. L. 2011, GCN Circular, 12633
- Klotz, A., Gendre, B., Stratta, G., et al. 2006, *A&A*, **451**, 39
- Kobayashi, S. 2000, *ApJ*, **545**, 807
- Kong, S. W., Wong, A. Y. L., Huang, Y. F., & Cheng, K. S. 2010, *MNRAS*, **402**, 409
- Kouveliotou, C., Meegan, C. A., Fishman, G. J., et al. 1993, *ApJL*, **413**, L101
- Kruhler, T. 2011, *IAU Symp*, **279**, 46
- Kruhler, T., Greiner, J., McBreen, S., et al. 2009, *ApJ*, **697**, 758
- Kumar, P., & Panaitescu, A. 2000, *ApJL*, **541**, L51
- Lazzati, D., Rossi, E., Covino, S., Ghisellini, G., & Malesani, D. 2002, *A&A*, **396**, 5
- Levan, A. J., Tanvir, N. R., Starling, R. L. C., et al. 2013, arXiv:1302.2352L
- Levesque, E. M. 2013, arXiv:1302.4741
- Li, Z., & Waxman, E. 2008, *ApJ*, **674**, 65
- Liang, E. W., Li, L., Gao, H., et al. 2013, *ApJ*, **774**, 13
- Liang, E. W., Yi, S.-X., Zhang, J., et al. 2010, *ApJ*, **725**, 2209
- MacFadyen, A. I., & Woosley, S. E. 1999, *ApJ*, **524**, 262
- Margutti, R., Bernardini, G., Barniol Duran, R., et al. 2011, *MNRAS*, **410**, 1064
- Morgan, A. N., et al. 2013, arXiv:1305.1928v1
- Nakauchi, D., et al. 2013, arXiv:1307.5061v1
- Oates, S., Page, M. J., Schady, P., et al. 2009, *MNRAS*, **395**, 490
- Paczynski, B. 1998, *ApJL*, **494**, L45
- Palmer, D. M., Barthelmy, S. D., Baumgartner, W. H., et al. 2011, GCN Circular, 12640
- Panaitescu, A., & Kumar, P. 2000, *ApJ*, **543**, 66
- Pei, Y. C. 1992, *ApJ*, **395**, 130
- Peng, F., Königl, A., & Granot, J. 2005, *ApJ*, **626**, 966
- Penacchioni, A. V., Ruffini, R., Bianco, C. L., et al. 2013, *A&A*, **551**, 133
- Penacchioni, A. V., Ruffini, R., Izzo, L., et al. 2012, *A&A*, **538**, 58
- Pisani, G. B., Izzo, L., Ruffini, R., et al. 2013, *A&A*, **552**, L5
- Podsiadlowski, P. 1992, *PASP*, **104**, 717
- Podsiadlowski, P., Ivanova, N., Justham, S., & Rappaport, S. 2010, *MNRAS*, **406**, 840
- Poole, T. S., Breeveld, A. A., Page, M. J., et al. 2009, *MNRAS*, **383**, 627
- Predehl, P., & Schmitt, J. H. M. M. 1995, *A&A*, **293**, 889
- Quataert, E., & Kasen, D. 2012, *MNRAS*, **419**, L1
- Ruffini, R., Bianco, C. L., Frascchetti, F., Xue, S.-S., & Chardonnet, P. 2001, *ApJL*, **555**, L117
- Sakamoto, T., Barthelmy, S. D., Baumgartner, W. H., et al. 2010, GCN Circular, 11169
- Sari, R., Piran, T., & Narayan, R. 1998, *ApJ*, **197**, 17
- Schady, P., Page, M. J., Oates, S. R., et al. 2010, *MNRAS*, **401**, 2773
- Schlegel, D. J., Finkbeiner, D. P., & Davis, M. 1998, *ApJ*, **500**, 502
- Stratta, G., Fiore, F., Antonelli, L. A., Piro, L., & De Pasquale, M. 2004, *ApJ*, **608**, 846
- Thöne, C. C., de Ugarte Postigo, A., Fryer, C. L., et al. 2011, *Natur*, **480**, 72
- Vreeswijk, P., Fynbo, J., & Melandri, A. 2011, GCN Circular, 12648
- Waxman, E., & Draine, B. T. 2000, *ApJ*, **537**, 796
- Woosley, S. E. 1993, *ApJ*, **405**, 273, GCN Circular, 12648
- Woosley, S. E., & Bloom, J. S. 2006, *ARA&A*, **44**, 507
- Woosley, S. E., & Heger, A. 2012, *ApJ*, **752**, 32
- Wu, X.-F., Hou, S.-J., & Lei, W.-H. 2013, *ApJL*, **767**, L36
- Zauderer, B. A., Berger, E., Margutti, R., et al. 2013, *ApJ*, **767**, 161
- Zhang, B. B., Zhang, B., Liang, E.-W., et al. 2011, *ApJ*, **730**, 141